Mapping Radiation Injury and Recovery in Bone Marrow Using ^{18}F-FLT PET/CT and USPIO MRI in a Rat Model

David A. Rendon*[1], Khushali Kotedia*[1], Solmaz F. Afshar[2], Jyotinder N. Punia[3], Omaima M. Sabek[2], Beverly A. Shirkey[4], Janice A. Zawaski[1], and M. Waleed Gaber[1]

[1]Hematology-Oncology Section, Department of Pediatrics, Baylor College of Medicine, Houston, Texas; [2]Department of Surgery, Houston Methodist Hospital Research Institute, Houston, Texas; [3]Department of Pathology and Immunology, Baylor College of Medicine, Houston, Texas; and [4]Center for Outcomes Research, Department of Surgery, Houston Methodist Hospital Research Institute, Houston, Texas

We present and test the use of multimodality imaging as a topological tool to map the amount of the body exposed to ionizing radiation and the location of exposure, which are important indicators of survival and recovery. To achieve our goal, PET/CT imaging with 3′-deoxy-3′-^{18}F-fluorothymidine (^{18}F-FLT) was used to measure cellular proliferation in bone marrow (BM), whereas MRI using ultra-small superparamagnetic iron oxide (USPIO) particles provided noninvasive information on radiation-induced vascular damage. **Methods:** Animals were x-ray–irradiated at a dose of 7.5 Gy with 1 of 3 radiation schemes—whole-body irradiation, half-body shielding (HBS), or 1-leg shielding (1LS)—and imaged repeatedly. The spatial information from the CT scan was used to segment the region corresponding to BM from the PET scan using algorithms developed in-house, allowing for quantification of proliferating cells, and BM blood volume was estimated by measuring the changes in the T_2 relaxation rates (ΔR_2) collected from MR scans. **Results:** ^{18}F-FLT PET/CT imaging differentiated irradiated from unirradiated BM regions. Two days after irradiation, proliferation of 1LS animals was significantly lower than sham ($P = 0.0001$, femurs; $P < 0.0001$, tibias) and returned to sham levels by day 10 ($P = 0.6344$, femurs; $P = 0.3962$, tibias). The degree of shielding affected proliferation recovery, showing an increase in the irradiated BM of the femurs, but not the tibias, of HBS animals when compared with 1LS ($P = 0.0310$, femurs; $P = 0.5832$, tibias). MRI of irradiated spines detected radiation-induced BM vascular damage, measured by the significant increase in ΔR_2 2 d after whole-body irradiation ($P = 0.0022$) and HBS ($P = 0.0003$) with a decreasing trend of values, returning to levels close to baseline over 10 d. Our data were corroborated using γ-counting and histopathology. **Conclusion:** We demonstrated that ^{18}F-FLT PET/CT and USPIO MRI are valuable tools in mapping regional radiation exposure and the effects of radiation on BM. Analysis of the ^{18}F-FLT signal allowed for a clear demarcation of exposed BM regions and elucidated the kinetics of BM recovery, whereas USPIO MRI was used to assess vascular damage and recovery.

Key Words: radiation; bone marrow; proliferation; ^{18}F-FLT PET/CT; USPIO-MRI

In the aftermath of a nuclear disaster, a victim's total dose and degree of radiation exposure will be a complicated function of their distance from the source of radiation and the presence of shielding factors in direct line to that source (*1*). The severity of radiation injury depends in part on the total dose absorbed, amount of the body that is exposed, and the anatomic region that has been irradiated. The extent of radiation exposure will result in marked differences in the victim's survival probability, their medical management, and their acute and late prognosis, necessitating long-term monitoring of all survivors, with some requiring immediate medical attention (*2*). Furthermore, in radiotherapy for cancer patients, bone marrow (BM) toxicity can be a limiting factor in determining therapeutic radiation doses. Although medical imaging is at the forefront of early diagnosis of disease and patient triaging, imaging is not yet an integrated tool in emergency preparedness plans in response to a nuclear disaster (*3*). In this article, we address this issue by making use of 3′-deoxy-3′-^{18}F-fluorothymidine (^{18}F-FLT) PET/CT and ultra-small superparamagnetic iron oxide (USPIO) MRI in a rat model of whole- and partial-body radiation exposure to measure BM proliferation and vascular damage as surrogates for mapping the amount of body exposed and the anatomic region irradiated. BM occupies interstices within the bones distributed throughout the entire skeleton and is one of the most proliferative and radiosensitive organs in the body, with a highly vascularized network of thin-walled, fenestrated sinusoidal endothelial cells (*4*).

This microvasculature, forming the blood–bone marrow barrier (BMB), serves as a gatekeeper regulating the passage of hematopoietic cells between the marrow and the circulation and is susceptible to the effects of radiation, displaying signs of necrosis, marked dilation, and damage, with plasma and red blood cell leakage into the BM parenchyma (*5*). Whole-body irradiation (WBI) is used as a conditioning regimen for BM transplantation by disrupting the BMB, facilitating the passage of transplanted cells and suppressing their rejection through its myeloablation effects.

^{18}F-FLT is a thymidine analog that is phosphorylated by thymidine kinase 1 during DNA synthesis, becoming trapped within the cell (*6*). Accumulation of ^{18}F-FLT is greater in proliferating tissues, making it ideal for its use in imaging BM and the effect of irradiation on its proliferation (*7*). USPIOs have a long blood half-life (*8*) and they alter the T_2 relaxation, causing a signal loss between normal and damaged tissue, which can be caused by an increase in blood volume, such as what occurs in the radiation-induced
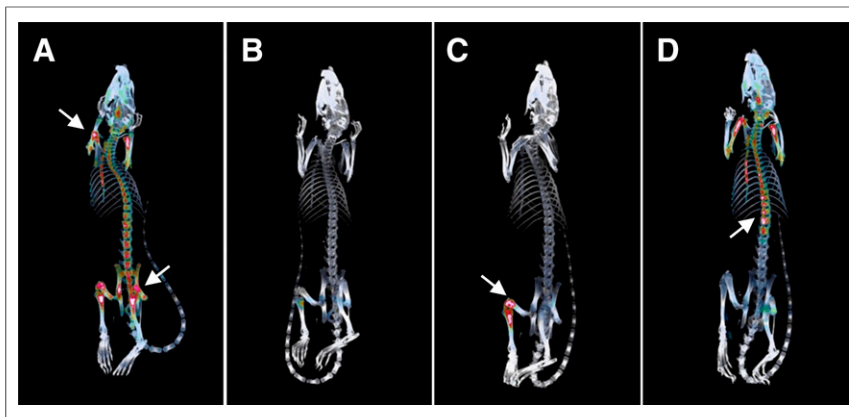
FIGURE 1. ^{18}F-FLT PET/CT imaging maps degree and location of radiation exposure. Reconstructed PET/CT images showing sites of radiation injury in rat with sham irradiation (A), WBI (B), 1LS (C), and HBS (D). Arrows point to examples of hot spots where ^{18}F-FLT was taken up.

^{18}F-FLT PET/CT Imaging

CT and PET scans were obtained using undocked Inveon scanners (Siemens AG). Because of imaging-field limitations of the scanner in obtaining full-body scans of a rat, the scans were divided into 2 sessions: the first covering the upper part of the body to the mid abdomen and the second covering the lower part. Before scanning, each animal was injected intravenously with thymidine phosphorylase (1.3 units/g; Sigma-Aldrich Co.), to reduce the serum levels of endogenous thymidine (9). Forty-five minutes after thymidine phosphorylase injection, the rat was injected intravenously with 12.58 MBq (340 μCi) of ^{18}F-FLT (Cyclotope). Rats were anesthetized with 2% isoflurane in oxygen, adjusted to maintain a rate of 30–40 breaths/min, and placed prone inside a half-cut plastic bottle (Ozarka; Nestlé Waters North America, Inc.) to allow for manipulation of the animal while maintaining its position, with a respiration pad (BioVet) to monitor the animal continuously. First, a CT scan was acquired using the following protocol: 2 bed positions, each of which contained 220 acquired projections covering 220°, with a source-to-detector distance of 328.91 mm and a source-to-center of rotation distance of 263.92 mm. The x-ray tube voltage and current were set at 80 kVp and 500 μA, respectively, with an exposure time of 180 ms per projection. The animal was imaged for 20 min starting 1 h after injection of ^{18}F-FLT. The bottle was then rotated 180° to scan the lower part of the body using the same protocol as described above. The scans were positioned to have an overlap to help produce a complete rat body scan. The spatial information from the CT scan was used to segment the region corresponding to BM from the PET scan using algorithms developed in-house (Supplemental Video 1; supplemental materials are available at http://jnm.snmjournals.org), as described in the supplement.

disruption of BMB integrity, resulting in the extravasation of the particles into the parenchyma.

In this work, we used a rat model with various degrees of radiation exposure to demonstrate the feasibility of our paradigm by making use of ^{18}F-FLT, a proliferation molecular agent, and USPIO, a magnetic contrast agent, to measure radiation-induced BM eradication and BMB disruption, its topological location, and kinetics of recovery.

MATERIALS AND METHODS

Animal Irradiation

All animal experiments were performed in accordance with the regulations of the Institutional Animal Care and Use Committee at Baylor College of Medicine. For the PET/CT studies, 5- to 6-wk-old male Sprague–Dawley rats (Harlan Laboratories) were divided into 4 groups: a control group that received no radiation (sham), whole-body irradiation (WBI), half-body shielding (HBS), or 1-leg shielding (1LS). To ensure MR field homogeneity, small-sized male Fischer 344 rats (Harlan Laboratories) aged 6–7 wk were used for the MR studies and were either WBI or HBS. All animals were anesthetized with isoflurane (2%) in oxygen, positioned prone, and x-ray–irradiated with 7.5 Gy (RS 2000 x-ray irradiator; Rad Source Technologies) at a dose rate of 1.16 Gy/min. Shielding was accomplished using 0.5-cm-thick slabs of malleable lead covering the entire leg or half of the animal's body of 1LS or HBS animals, respectively.

γ-Counter Measurements

Cell proliferation measurements using ^{18}F-FLT PET/CT were corroborated using a γ-counter (Wizard[2] 2480; PerkinElmer). Animal experiments followed the same protocol as previously described for injections of thymidine phosphorylase and ^{18}F-FLT. To standardize the time allowed for ^{18}F-FLT uptake, tissue-harvesting times reproduced the

TABLE 1
Distribution of BM in Sham Rats

Anatomical region	Volume (mL)	Total volume (%)	Average SUV	Aggregate SUV	Total SUV (%)
Skull	2.432 ± 0.057	24.97	0.442 ± 0.020	8,976.79 ± 468.00	13.21
Arms/hands/shoulders	1.335 ± 0.046	13.71	0.813 ± 0.040	9,033.61 ± 486.20	13.30
Sternum	0.123 ± 0.006	1.26	1.307 ± 0.102	1,327.54 ± 91.79	1.95
Backbone	2.093 ± 0.091	21.49	0.968 ± 0.049	16,887.17 ± 1,105.65	24.86
Hips	0.710 ± 0.039	7.29	1.282 ± 0.062	7,562.37 ± 483.09	11.13
Femurs	0.807 ± 0.038	8.28	1.383 ± 0.084	9,275.22 ± 651.04	13.65
Tibias	0.834 ± 0.036	8.56	1.144 ± 0.074	7,946.37 ± 618.99	11.70
Whole body	9.741 ± 0.364	100.00	0.838 ± 0.042	67,929.80 ± 3,978.95	100.00

Values do not include the tail. Values are presented as mean ± SE. Animal number, $n = 6$.
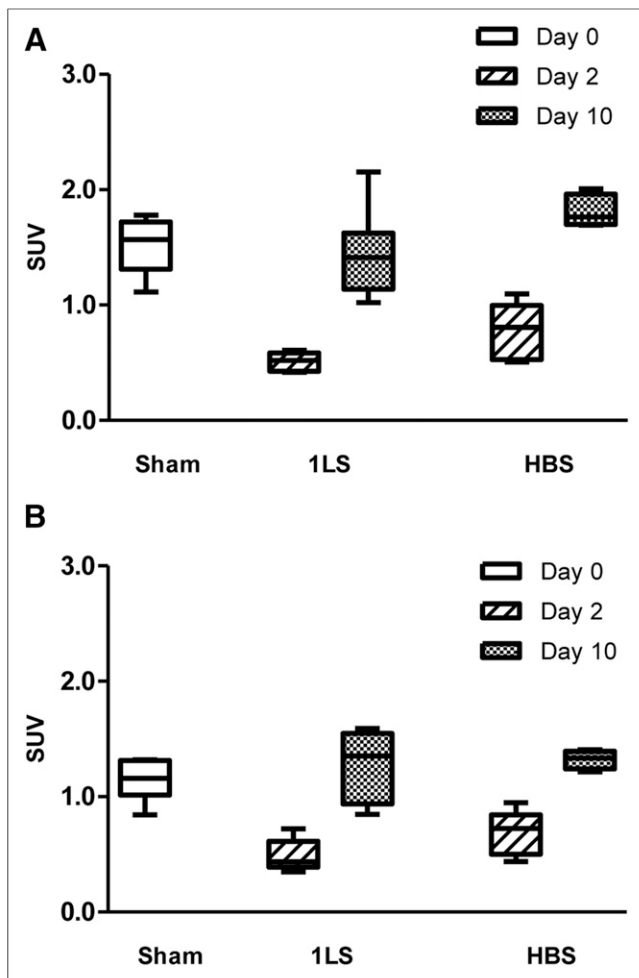
FIGURE 2. ^{18}F-FLT PET/CT data demonstrate clear effect of radiation exposure on BM proliferation. Box plot of average SUV of irradiated femur (A) and tibia (B) at 2 and 10 d after exposure.

same time frame used in the PET/CT imaging studies. The legs of the animal were isolated, and the ^{18}F-FLT radioactivity in the femurs, tibias, and blood was counted, corrected for the radionuclide decay to the time of injection, and normalized to the injected dose and weight of the tissue.

In Vivo MRI

MR images were acquired using a Bruker BioSpec 94/20 operating at 9.4 T and equipped with a 200 mT/m gradient coil insert. A 72-mm linear birdcage resonator was used for radiofrequency transmission, and a 2-cm-diameter surface coil, used in the receive-only mode, was placed on the lateral surface of the spine covering vertebrae T11-L1. MR images were acquired using Bruker's PARAVISION 5.1 software. A respiratory sensor pillow (SA Instruments) was placed on the abdomen of the animals to gate each spin-echo to the same position in the respiratory cycle and to monitor the respiration rate. Respiration of the animal was maintained at 30 breaths/min by a mixture of 2% isoflurane in oxygen. Body temperature was maintained at 37°C by a recirculating water system incorporated in the animal bed. The animals were placed prone in the scanner with the head stabilized by a teeth holder and secured to the cradle. A T2-weighted rapid acquisition with relaxation enhancement (RARE) sequence was used to acquire sagittal anatomic images using the following parameters: repetition time/echo time, 2,000/17.6 ms; RARE factor, 4; slice

thickness, 0.8 mm; slices, 3; number of excitations, 6; matrix dimensions, 256×256; and field of view, 3×3 cm, giving an in-plane resolution of 117×117 μm². After localizer acquisitions, 4 axial slices through the BM were selected for susceptibility contrast MRI (Supplemental Fig. 1). To measure the change in relaxation rate, ΔR_2, as described by Boxerman et al. (10), a T2-weighted RARE sequence was performed before and after administration of ferumoxytol (4 mg Fe/kg) (Feraheme; AMAG Pharmaceuticals Inc.) intravenously, via a lateral tail vein catheter, using the following parameters: repetition time/echo time, 2,000/20.41 ms; RARE factor, 4; slice thickness, 1.5 mm; matrix size, 128×128; 2 averages; and field of view, 1.2×1.2 cm, giving an in-plane resolution of 94×94 μm². ΔR_2 color-coded relative blood volume maps were calculated using customized scripts in MATLAB (The MathWorks), as described in the supplemental materials.

Histopathologic Analysis

BM specimens were fixed in 10% buffered formalin for 48 h and decalcified (TBD-2 Decalcifier; Thermo Scientific) for 72 h. Paraffin-embedded tissue was cut in 4-μm sections and stained with 1 of 3 stains: hematoxylin and eosin (H&E); factor VIII (FVIII), an immunohistochemical stain marking endothelial cells, megakaryocytes, and platelets; or bromodeoxyuridine, a thymidine analog used to label cells in the S-phase of DNA synthesis, injected 4 h before euthanization. BM smears were also collected for Prussian blue staining to detect the presence of iron.

Statistical Analysis

Data were presented as mean and SD of the means. Group means were compared using a Student t test. When comparing irradiated with sham legs, paired t tests were used, assuming unequal variances. A linear model adjusting for the repeated measures on each animal was used to analyze the MR data. Statistical significance was assigned for a P value less than 0.05. All statistical computations were processed using Stata 13.1 for Windows (StataCorp LP).

RESULTS

Proliferation

^{18}F-FLT PET/CT Imaging. Imaging can differentiate irradiated from unirradiated BM regions throughout the body (Fig. 1). The backbone (total standardized uptake value [SUV], 24.86%) contained the largest amount of proliferating BM, followed by the lower and upper limbs, whereas the femur had the highest proliferation per unit volume (Table 1). Our PET data demonstrated a clear effect of radiation exposure on BM proliferation (Fig. 2). Measured by SUV, proliferation was significantly lower in the irradiated femurs of the 1LS group ($P = 0.0001$) 2 d after irradiation (0.51 ± 0.076, $n = 6$) than the sham group (1.52 ± 0.247, $n = 6$) (Fig. 2A). Similarly, proliferation was significantly lower ($P < 0.0001$) in the irradiated tibias of the 1LS group (0.49 ± 0.133, $n = 8$) than the sham group (1.14 ± 0.181, $n = 6$) (Fig. 2B). Ten days after exposure, proliferation was restored to control levels whereby both the irradiated femurs and the tibias of the 1LS group (1.44 ± 0.362 and 1.26 ± 0.301, $n = 8$, respectively) were statistically equal to their sham equivalent ($P = 0.6344$ and 0.3962, respectively). Considering the effects of the degree of shielding on recovery by day 10, the irradiated tibias from the 1LS group were not significantly different ($P = 0.5832$) from the irradiated tibias of the HBS group (1.32 ± 0.081, $n = 4$), possibly because of the minimal amount of BM in the tissue. However, the irradiated femurs of the 1LS group differed significantly ($P = 0.0310$) from the irradiated femurs of the HBS group (1.81 ± 0.145, $n = 4$), suggesting a significant dependence in recovery of BM proliferation
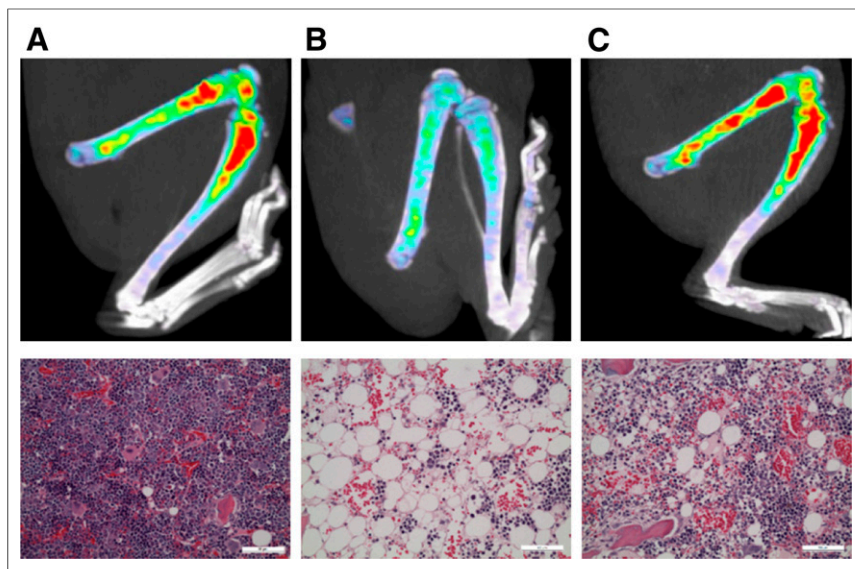
FIGURE 3. Proliferation drastically decreases immediately after radiation exposure. PET/CT (top) and H&E (bottom) images of sham irradiated leg and HBS (A) at 2 d (B) and 10 d (C) after irradiation.

on the amount of BM exposed, with greater robustness as the amount of shielded BM increased.

γ-Counting. As in the PET data, the accumulation of ^{18}F-FLT in sham blood, femurs, and tibias (0.00091 ± 0.000078, 0.00897 ± 0.001596, and 0.00653 ± 0.001047 percentage injected dose per gram [%ID/g], respectively) was significantly different ($P < 0.0001$) from that of irradiated blood, femurs, and tibias of 1LS animals (0.00072 ± 0.000163, 0.00112 ± 0.000406, and 0.00098 ± 0.000389 %ID/g, respectively) 2 d after radiation exposure.

Histopathology. To further corroborate our findings with other measures of proliferation, we stained femur sections with H&E (Fig. 3; Supplemental Fig. 2) and bromodeoxyuridine (Supplemental Fig. 3) at 2 and 10 d after irradiation. Sham tissue showed structured, cellularly dense, and highly proliferative BM, whereas at 2 d after radiation exposure the BM showed a subtotal loss of hematopoietic cells, massive hemorrhaging, a loss of structure with no osteoblasts bordering the marrow along the bone, and a drastic loss in proliferation, similar to what was observed in our ^{18}F-FLT studies. Although at 10 d after exposure the BM showed signs of regaining its organized structure and revitalization in proliferation, there were indications of persistent damage evidenced by the presence of adipose tissue.

Vascularity

MRI. A heat mask generated at various time points after radiation exposure (Supplemental Fig. 4) showed a visual map of the changes in the relaxation rate, ΔR_2, after injury and up to 10 d thereafter. Using linear regression analysis, we observed that within a particular experimental group (WBI and HBS), ΔR_2 (S^{-1}) changed significantly over time. Two days after WBI (38.69 ± 7.65), there was a significant increase ($P = 0.0004$) in ΔR_2 (Fig. 4) when compared with baseline (17.38 ± 3.03), which remained significant at day 5 (26.50 ± 7.79, $P = 0.0479$), with a gradual decrease back to nonsignificant values by day 7 (13.47 ± 5.25, $P = 0.7693$) and day 10 (11.03 ± 3.70, $P = 0.5473$). To test whether BM shielding had any positive effect on vascular damage, we shielded half of the animals' bodies and measured vascular changes in the same irradiated vertebral region.

Two days after HBS, there was a significant increase (37.17 ± 1.95, $P < 0.0001$) in ΔR_2 (Fig. 4) when compared with baseline (10.31 ± 4.31), which stayed significant at day 5 (21.38 ± 4.81, $P = 0.0220$), with a gradual decrease back to values insignificant from sham by day 7 (11.42 ± 4.73, $P = 0.0852$) but dipping significantly below sham at day 10 (8.48 ± 3.85, $P = 0.0118$). Adjusting for repeated measures within the rats and time points, the average effect of WBI versus HBS was an increase of 3.7.

Histopathology. The H&E-stained sections of sham vertebrae (Fig. 5A, top) showed normal BM architecture. The background stroma showed small, intact caliber blood vessels, highlighted by a positive brown hue in the immunohistochemical stain for FVIII (Fig. 5A, bottom). Two days after WBI exposure (Fig. 5B), there was markedly hypocellular marrow with prominent stromal damage, including extravasation of red blood cells and dilated and disrupted blood vessels. Seven days after exposure (Fig. 5C), there was still markedly hypocellular marrow whereas adipose tissue increased to fill the marrow space, with extravasated red blood cells still present and hematopoietic cells almost absent. This same trend persisted for 10 d, where BM remained markedly hypocellular and the marrow replaced by adipose tissue (Fig. 5D). However, by this time, the stroma appeared to be recovering; scant extravasated red blood cells, no large irregular blood vessels, and rare small aggregates of hematopoietic cells were seen. We scored these H&E sections (Table 2) and found that the highest score for hemorrhage was at 2 d after exposure. Two days after HBS, the exposed vertebral sections demonstrated the same features as WBI BM (Supplemental Fig. 5A), with extravasated iron particles as shown in the Prussian blue–stained BM smears (Supplemental Fig. 6). However, at day 10 the BM showed signs of recovery, with a significant number of hematopoietic cells and vascular reconstruction (Supplemental Figs. 5 and 6C).
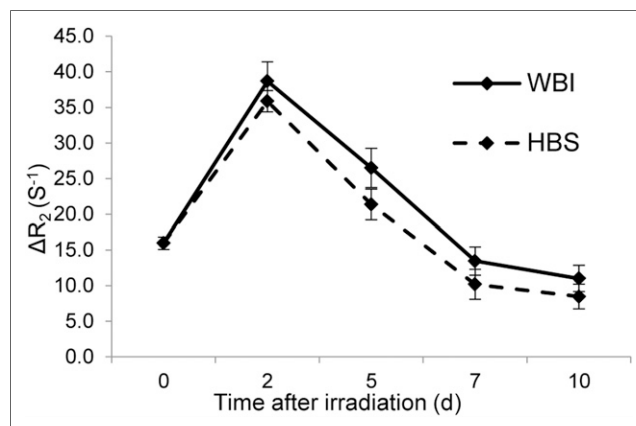

FIGURE 4. Radiation-induced damage to BMB and microvascular network showing increased hemorrhaging, as measured with USPIO MRI. Average changes in relaxation rate, ΔR_2, of WBI or HBS rats at 2, 5, 7, and 10 d after irradiation.
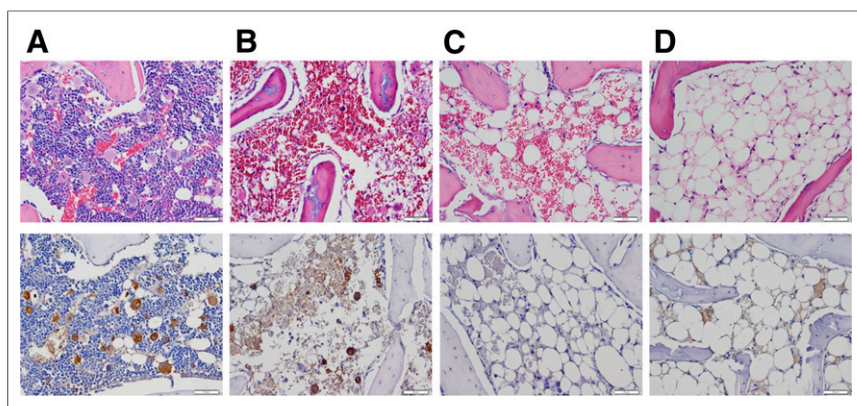
FIGURE 5. Immunohistochemical evidence of radiation-induced vascular damage. Representative images of spines stained for H&E (top) and FVIII (bottom; brown hue) at sham (A), 2 d (B), 7 d (C), and 10 d after WBI (D).

DISCUSSION

Our results demonstrated that imaging not only can differentiate irradiated from unirradiated BM regions but also can measure BM recovery. ^{18}F-FLT PET/CT imaging can map the degree and location of radiation exposure, whereas USPIO MRI can be used to measure radiation-induced vascular damage. We also observed that the amount of BM proliferation, but not vascular recovery, in irradiated regions is significantly dependent on the degree of body exposed. Using γ-counting measurements, we verified that the signal obtained from the PET scans of BM was independent of our imaging procedures. Immunohistochemical staining demonstrated that proliferation was affected by radiation exposure in a manner similar to our ^{18}F-FLT measurements, as was vascular integrity, determined from our MR data.

^{18}F-FLT PET/CT imaging demonstrated a radiation-induced reduction in proliferation at 2 d after exposure (Fig. 2), which was restored to near-control levels by day 10. This observation was confirmed histologically using H&E staining as a measure of progenitor cell density (Fig. 3; Supplemental Fig. 2) and bromodeoxyuridine staining of proliferative cells (Supplemental Fig. 3). In our analysis, we distinguished equal volumes of active BM from different bones, and further from different regions within the bone. From our measurements, we derived 2 distinct values that provided information about the BM in the region of interest: an average activity (average SUV), which indicated the average rate of proliferation throughout the volume, and the integration of that average activity (total SUV), which specified the total proliferation. The first value was indicative of the degree of participation and demand for proliferating BM cells in hematopoiesis, whereas the second value represented the total amount of proliferating cells in a given region. The sternum was a prime example of how these 2 measurements provided us with additional information on BM activity: its average SUV was one of the highest, but because of its small volume it contributed less than 2% of the total SUV of the body. From the total SUV, we determined that most of the BM activity was concentrated in the backbone, femurs, skull, and tibias (Table 1), agreeing with Shaposhnikov et al. (11), who reported that the highest cell counts from BM biopsies were found, in descending order, in the backbone, skull, pelvis, femur, and tibia. Together, the average and total SUV can be used in a victim's triaging in the event of a nuclear disaster and when making decisions on the use of radiation therapy or cytotoxic drugs in the treatment planning of malignant diseases (12).

Our results are also partially consistent with previous works that directly measure the distribution of BM in humans, with the major discrepancy being the percentage of BM in the limbs. Ellis et al. (13) measured a relatively low amount of red BM in the proximal ends of the femur and humerus, with negligible amounts in the rest of the limbs, whereas we observed that the femurs and tibias contain a quarter of BM activity in unirradiated rats (13.7% and 11.7%, respectively) as well as an appreciable activity in the arms. Aside from the obvious difference in species, this discrepancy can be explained by the age of these adolescent rats, in comparison to the human data, which was taken from adult subjects, because red BM recedes with age (14).

Radiation exposure not only reduces the progenitor cell population and its proliferative activity, but also damages the BMB and the sinusoidal architecture necessary for the continued production and delivery of hematopoietic cells (4). Our USPIO MRI data, confirmed by immunohistochemical staining (Fig. 5), show a clear indication of radiation-induced vascular hemorrhage (H&E) and a loss of vascular integrity (FVIII), with a peak at 2 d after exposure that subsides by day 10. The kinetics of vascular response in both the imaging and the histologic data coincide, demonstrating the ability of USPIO MRI to measure radiation-induced vascular disruption. Further, the disruption did not differ significantly between radiation schemes 2 d after exposure (Fig. 5; Supplemental Fig. 5). Philippens et al. have demonstrated the presence of USPIO particles in the irradiated rat spinal cord using Prussian blue staining and the corresponding MRI signal intensity changes induced by its presence (15). Daldrup et al. (16) used electron microscopy to detect USPIO particles in the BM, and in a different study they showed that the MR dynamic signal increased significantly 1–2 d after total-body irradiation, which is consistent with our data (17). Further, Fliender et al. (4) and others have reported that revascularization of BM after irradiation is necessary for hematopoietic regeneration, as also supported by our data, which showed that vascular recovery coincided with increased hematopoiesis.

One main concern in the use of PET/CT imaging is the perceived damaging effect of exposing radiation victims to further radiation. However, the accuracy and sensitivity that such imaging

TABLE 2
Histologic Scoring of Hemorrhage

Blood cell extravasation score	Sham	Day 2	Day 7	Day 10
%N(0)	66.7	0	0	33.3
%N(1)	33.3	0	33.3	66.7
%N(2)	0	33.3	66.7	0
%N(3)	0	66.7	0	0
N	3	3	3	3

examinations provide would outweigh these risks, given the comparatively small dose of ^{18}F-based radiopharmaceuticals needed for PET imaging (18). Additionally, CT scans associated with PET studies are intended only for PET attenuation correction and anatomic localization of the activity of the radiotracer, whose doses are usually estimated to be only two thirds or less of the doses delivered by the PET scan (18).

CONCLUSION

Our goal was to investigate the possibility of using medical imaging techniques to design and implement a triaging system that can be used in a nuclear incident or accidental exposure. We presented data that demonstrated the use of imaging to delineate the radiation-exposed regions of BM and the effect of shielding on its recovery. Our goal was achieved using ^{18}F-FLT PET/CT to record changes in proliferation and the utility of USPIO MRI in monitoring vascular changes. These tools can be used to distinguish the extent of bodily exposure and in the long-term management of radiation victims and radiotherapy patients.

DISCLOSURE

ACKNOWLEDGMENTS

REFERENCES

1. Knebel AR, Coleman CN, Cliffer KD, et al. Allocation of scarce resources after a nuclear detonation: setting the context. *Disaster Med Public Health Prep.* 2011;5(suppl 1):S20–S31.
2. Dörr HD, Meineke V. Appropriate radiation accident medical management: necessity of extensive preparatory planning. *Radiat Environ Biophys.* 2006;45:237–244.
3. Murrain-Hill P, Coleman CN, Hick JL, et al. Medical response to a nuclear detonation: creating a playbook for state and local planners and responders. *Disaster Med Public Health Prep.* 2011;5(suppl 1):S89–S97.
4. Fliedner TM, Graessle D, Paulsen C, Reimers K. Structure and function of bone marrow hemopoiesis: mechanisms of response to ionizing radiation exposure. *Cancer Biother Radiopharm.* 2002;17:405–426.
5. Kopp HG, Avecilla ST, Hooper AT, Rafii S. The bone marrow vascular niche: home of HSC differentiation and mobilization. *Physiology (Bethesda).* 2005;20:349–356.
6. Rasey JS, Grierson JR, Wiens LW, Kolb PD, Schwartz JL. Validation of FLT uptake as a measure of thymidine kinase-1 activity in A549 carcinoma cells. *J Nucl Med.* 2002;43:1210–1217.
7. Agool A, Slart RH, Thorp KK, et al. Effect of radiotherapy and chemotherapy on bone marrow activity: a ^{18}F-FLT-PET study. *Nucl Med Commun.* 2011;32:17–22.
8. Weissleder R, Elizondo G, Wittenberg J, Rabito CA, Bengele HH, Josephson L. Ultrasmall superparamagnetic iron oxide: characterization of a new class of contrast agents for MR imaging. *Radiology.* 1990;175:489–493.
9. van Waarde A, Cobben DC, Suurmeijer AJ, et al. Selectivity of ^{18}F-FLT and ^{18}F-FDG for differentiating tumor from inflammation in a rodent model. *J Nucl Med.* 2004;45:695–700.
10. Boxerman JL, Hamberg LM, Rosen BR, Weisskoff RM. MR contrast due to intravascular magnetic susceptibility perturbations. *Magn Reson Med.* 1995;34:555–566.
11. Shaposhnikov VL. Distribution of the bone marrow cells in the skeleton of mice [in Russian]. *Biull Eksp Biol Med.* 1979;87:483–485.
12. McGuire SM, Menda Y, Boles Ponto LL, Gross B, Buatti J, Bayouth JE. 3′-deoxy-3′-[^{18}F]fluorothymidine PET quantification of bone marrow response to radiation dose. *Int J Radiat Oncol Biol Phys.* 2011;81:888–893.
13. Ellis RE. The distribution of active bone marrow in the adult. *Phys Med Biol.* 1961;5:255–258.
14. Mauch P, Botnick LE, Hannon EC, Obbagy J, Hellman S. Decline in bone marrow proliferative capacity as a function of age. *Blood.* 1982;60:245–252.
15. Philippens ME, Gambarota G, Pikkemaat JA, Peeters WJ, van der Kogel AJ, Heerschap A. Characterization of late radiation effects in the rat thoracolumbar spinal cord by MR imaging using USPIO. *MAGMA.* 2004;17:303–312.
16. Daldrup HE, Link TM, Blasius S, et al. Monitoring radiation-induced changes in bone marrow histopathology with ultra-small superparamagnetic iron oxide (USPIO)-enhanced MRI. *J Magn Reson Imaging.* 1999;9:643–652.
17. Daldrup-Link HE, Link TM, Rummeny EJ, et al. Assessing permeability alterations of the blood-bone marrow barrier due to total body irradiation: in vivo quantification with contrast enhanced magnetic resonance imaging. *Bone Marrow Transplant.* 2000;25:71–78.
18. Leide-Svegborn S. Radiation exposure of patients and personnel from a PET/CT procedure with ^{18}F-FDG. *Radiat Prot Dosimetry.* 2010;139:208–213.